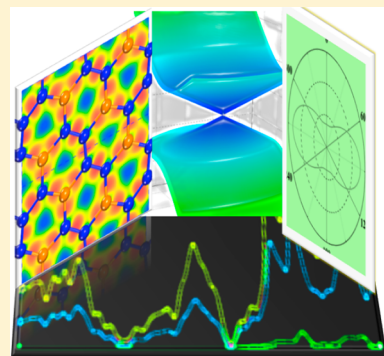


# A New Anisotropic Dirac Cone Material: A B<sub>2</sub>S Honeycomb Monolayer

Yu Zhao,<sup>1</sup> Xiaoyin Li, Junyi Liu, Cunzhi Zhang,<sup>1</sup> and Qian Wang<sup>\*1</sup>

Department of Materials Science and Engineering, Center for Applied Physics and Technology, College of Engineering, Peking University, Beijing 100871, China

**ABSTRACT:** Different from the isotropic Dirac cones existing in other two-dimensional (2D) materials, anisotropic Dirac cones have the merit of anisotropic carrier mobility for applications in direction-dependent quantum devices. Motivated by the recent experimental finding of an *anisotropic* Dirac cone in borophene, here we report a new 2D anisotropic Dirac cone material, B<sub>2</sub>S monolayer, identified by using a global structure search method and first-principles calculation combined with a tight-binding model. The B<sub>2</sub>S monolayer is found to be stable mechanically, thermally, and dynamically and exhibits an anisotropic Dirac cone exactly at the Fermi level, showing a Fermi velocity of 10<sup>6</sup> m/s in the same order of magnitude as that of graphene. Moreover, B<sub>2</sub>S monolayer is the first anisotropy Dirac cone material with a *pristine* honeycomb structure stabilized by S in free-standing conditions where each atom has four valence electrons on average being isoelectronic to C. This study would expand the Dirac cone material family with new features.



The passion for two-dimensional (2D) Dirac cone materials was ignited by graphene,<sup>1</sup> which is characterized by a linear energy dispersion at the Fermi level, exhibiting ballistic charge transport and ultrahigh carrier mobility.<sup>2</sup> Its Fermi velocity is as high as  $0.8 \times 10^6$  m/s, only 2 orders of magnitude lower than the velocity of light, offering a new way of developing electronic devices. The fascinating properties and vast applications displayed in graphene have stimulated a growing interest in studying 2D Dirac cone materials. Currently, extensive efforts have been devoted to silicene,<sup>3</sup> germanene,<sup>4</sup> carbon allotropes,<sup>5–8</sup> boron allotropes,<sup>9,10</sup> SiC<sub>3</sub>,<sup>11</sup> C<sub>4</sub>N,<sup>12</sup> and Be<sub>3</sub>C<sub>2</sub>,<sup>13</sup> which are identified as Dirac materials.

2D boron-based Dirac cone materials have attracted a lot of current attention because boron is positioned on the left side of carbon in the periodic table with a smaller covalent radius and the capacity of flexible bonding. For instance, it has been found that a Dirac cone can exist in a boron  $\beta_{12}$  monolayer<sup>14</sup> that was successfully synthesized<sup>15</sup> consisting of 5–6–7 boron rings,<sup>8</sup> triangular B chain-based porous sheet,<sup>7</sup> 8B-*Pmmn* borophene,<sup>16</sup> etc. Very recently, 2D anisotropic Dirac cones in  $\chi_3$  borophene were experimentally discovered by using high-resolution angle-resolved photoemission spectroscopy,<sup>17</sup> where the anisotropic Dirac cone exhibits anisotropic carrier mobility that may have advantages in direction-dependent transport for quantum devices. To date for all the reported 2D boron-based Dirac cone materials, their geometries are much more complicated than that of the *pristine* honeycomb structure of graphene because of the different electronic configuration of the boron atom, which has one fewer electron than carbon. The electron-deficient boron tends to form multiple center bonds in the 2D boron allotropes, where the  $p_z$  orbital is not dominating the interactions between electrons, which is different from the situation in graphene. Accordingly, the *pristine* honeycomb

geometry is unstable for a 2D B sheet in its freestanding state. Although it can be stabilized by adding two electrons to each boron hexagonal ring via doping metal atoms,<sup>18,19</sup> in all the metal-stabilized B sheets, metal atoms occupy all the intrinsic hexagonal hollow sites. Thus, the resulting geometries are very different from the simple honeycomb configuration of graphene.

In this work, we chose boron and sulfur for a B–S honeycomb monolayer because of their special electronic configurations and flexible bonding ability.<sup>20–31</sup> In addition, a binary compound with an atomic ratio greater than 1 could generate crystals with low symmetry compared with graphene<sup>32</sup> and might lead to the materials with anisotropic Dirac cones, thus providing Fermi velocities in practical devices that are more flexible and tunable than those of the isotropic Dirac cone.<sup>33–36</sup> On the basis of the global structure search and state-of-the-art theoretical simulations, we have identified a desirable B<sub>2</sub>S honeycomb monolayer with an anisotropic Dirac cone located at the high symmetric line in *k*-space. In this structure, each atom has four valence electrons on average making B<sub>2</sub>S isoelectronic to graphene, while the lower symmetry induced by the two different species of elements is responsible for the anisotropic Dirac cone.

**Computational Methods.** The ground-state structure of 2D B<sub>2</sub>S is predicted by using the particle swarm optimization (PSO) algorithm implemented in the CALYPSO package.<sup>37–42</sup> The population size and the number of generations are both set to 30 to ensure the convergence. The number of formula units per unit cell are set to be 1, 2, 3, and 4, corresponding to B<sub>2</sub>S,

**Received:** February 27, 2018

**Accepted:** March 25, 2018

**Published:** March 26, 2018

$B_4S_2$ ,  $B_6S_3$ , and  $B_8S_4$ , respectively. To accommodate the structure buckling, we set the buffering thickness to 0.1 Å.<sup>37</sup> Atomic structure optimization, total energy, and electronic structure calculations are performed based on density functional theory (DFT), as implemented in the Vienna ab initio simulation package (VASP).<sup>43</sup> The projector augmented wave (PAW) method<sup>44</sup> is employed to treat the interactions between ion cores and valence electrons with a kinetic energy cutoff of 450 eV. The first Brillouin zone is sampled by a  $6 \times 10 \times 1$   $k$ -point grid within the Monkhorst–Pack scheme.<sup>45</sup> The exchange–correlation potential is treated using the Perdew–Burke–Ernzerh (PBE) functional<sup>46</sup> within the generalized gradient approximation (GGA)<sup>47</sup> in most cases, while the HSE06<sup>48,49</sup> hybrid functional is used to obtain a more accurate electronic band structure. The atomic positions are fully relaxed until the energy and atomic forces converge to  $10^{-4}$  eV and  $10^{-2}$  eV/Å, respectively. A large vacuum space of 20 Å in the perpendicular direction of the sheet is used to avoid the interactions between periodic images. The finite displacement method implemented in the phonopy package<sup>50</sup> is used to calculate the phonon spectra. Ab initio molecular dynamics (AIMD) simulations are carried out to confirm the thermal stability. The tight-binding (TB) matrix elements are calculated by projecting Bloch states onto the maximally localized Wannier functions (MLWFs), using the Wannier90 package<sup>51</sup> interfaced with Quantum ESPRESSO.<sup>52</sup>

Through the global structure searching for a  $B_2S$  monolayer sheet, we obtain three energetically favorable monolayer  $B_2S$  phases. The optimized geometries and the relative energies with respect to the lowest energy (0 eV) are plotted in Figure 1a–c. All of them present a graphene-like honeycomb structure

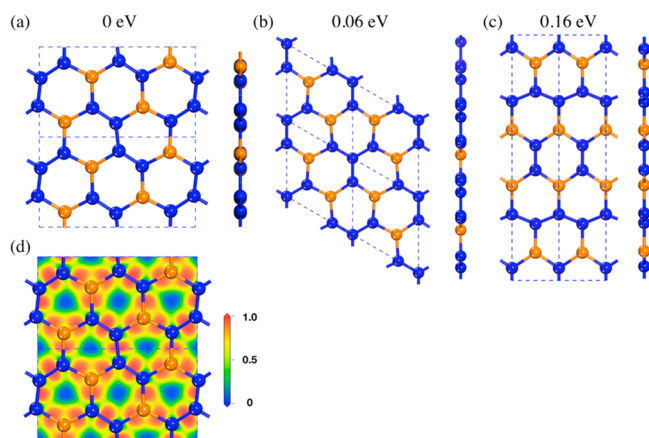


**Figure 1.** (a–c) Optimized low-lying energy geometries and (d) a slice (crossing the monatomic thick structure) of the electron localization function (ELF) of the  $B_2S$  monolayer.

without any buckling. The structure shown in Figure 1a is identified to be the most stable atomic configuration of the  $B_2S$  monolayer; the configuration shown in Figure 1a is 0.06 and 0.16 eV per  $B_2S$  formula unit lower in energy than the one shown in panels b and c of Figure 1, respectively. This structure has an orthogonal primitive cell (space group PBAM with a point group  $D_{2h}$ ) containing four formula units, with optimized lattice constants of  $a = 9.14$  Å,  $b = 5.26$  Å, and  $c = 20.88$  Å. All of the boron and sulfur atoms are three-coordinated, making it possible for their  $p_z$  orbitals to be conjugated. The hexagonal rings in the  $B_2S$  sheet are distorted with the bond angles ranging from  $114^\circ$  to  $123^\circ$  because B and S atoms have

different covalent radii and electronegativities. The bond lengths of B–B and B–S are 1.62 and 1.82 Å, respectively. This deviation from ideal honeycomb structure finally contributes to the anisotropic properties of this material, such as mechanical and electric properties.

To get more insight into the chemical bonding of the  $B_2S$  monolayer, we calculate its electron localization function (ELF)<sup>53</sup> to analyze the electron distribution. The ELF is a useful tool for chemical bond classification, which can be described in the form of a contour plot in real space with values renormalized between 0.00 and 1.00. The values of 1.00 and 0.50 correspond to fully localized and fully delocalized electrons, respectively, while the value 0.00 refers to very low charge density. The calculated results are plotted in Figure 1d, where the region with a large ELF value is portrayed in red, showing the paired electrons with local bosonic character and the strong covalent electron states of the  $\sigma$  bond formed by the  $sp^2$ -hybridized orbitals of B and S atoms.

To examine the stability of the  $B_2S$  monolayer, we first calculate its cohesive energy, which is defined by  $E_{\text{coh}} = -(E_{B_2S} - 8E_B - 4E_S)/12$ , where  $E_B$  and  $E_S$  are the total energies of a single B atom and single S atom, respectively, and  $E_{B_2S}$  is the total energy of a  $B_2S$  unit cell. Our calculated value is 5.3 eV/atom, which is comparable to that of some bulk boron sulfide phases recorded in the materials project data set,<sup>54</sup> including  $B_{12}S$  (5.8 eV/atom),  $B_2S_3$  (4.9 eV/atom), and  $BS_2$  (4.6 eV/atom), indicating that the  $B_2S$  sheet is energetically favorable. These cohesive energies are calculated at the same theoretical level.

We then examine the thermal stability of the  $B_2S$  sheet by performing AIMD simulations. A  $2 \times 3 \times 1$  supercell containing 72 atoms is adopted to reduce the constraint of the periodic boundary condition. The simulation is carried out with a Nosé–Hoover heat bath scheme<sup>55</sup> at 1000 K for 10 ps with a time step of 1 fs. The fluctuation of the total potential energy with simulation time is plotted in Figure 2b, which shows that the average value of the total potential energy remains nearly constant during the entire simulation. The structure of the  $B_2S$  monolayer at the end of the simulation is also plotted in Figure 2a, with no obvious structure collapse appearing. The above results indicate that the  $B_2S$  monolayer has good thermal stability and can maintain its structural integrity up to 1000 K. Therefore, this monolayer is thermally stable enough to withstand relatively high temperatures.

We also calculate the phonon spectra to check the dynamical stability of the  $B_2S$  monolayer. The calculated phonon dispersion curves are displayed in Figure 2b. The absence of an imaginary mode in the entire Brillouin zone confirms that the  $B_2S$  sheet is dynamically stable. Additionally, we further examine the mechanical stability of  $B_2S$  by calculating its linear elastic constants. The 2D linear elastic constants are calculated to be  $C_{11} = 150$  N·m<sup>−1</sup>,  $C_{22} = 160$  N·m<sup>−1</sup>,  $C_{12} = 32$  N·m<sup>−1</sup>, and  $C_{44} = 60$  N·m<sup>−1</sup>. The stability criteria for an orthorhombic 2D system are<sup>56</sup>

$$C_{11} > 0; C_{22} > 0; C_{44} > 0$$

$$C_{11}C_{22} > C_{12}^2$$

It is obvious that the elastic constants of the  $B_2S$  monolayer satisfy those conditions, confirming the mechanical stability of the sheet. Moreover, the in-plane Young's modulus and Poisson

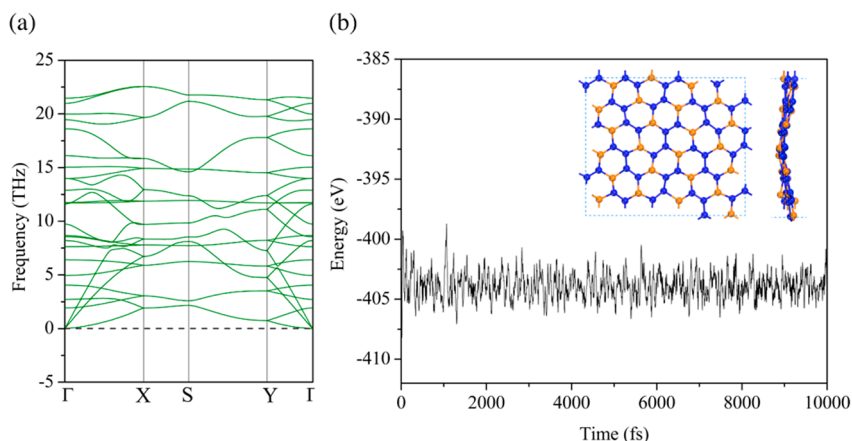


**Figure 2.** (a) Phonon spectra of the B<sub>2</sub>S monolayer. (b) Fluctuation of total potential energy of B<sub>2</sub>S monolayer during the AIMD simulation at 1000 K. The inset is the structure of B<sub>2</sub>S at the end of the AIMD simulation.

ratio along an arbitrary direction  $\theta$  ( $\theta$  is the angle relative to the positive  $x$  direction in the sheet) can be expressed as<sup>57</sup>

$$E(\theta) = \frac{C_{11}C_{22} - C_{12}^2}{C_{11}s^4 + C_{22}c^4 + \left(\frac{C_{11}C_{22} - C_{12}^2}{C_{44}} - 2C_{12}\right)c^2s^2}$$

$$\nu(\theta) = -\frac{\left(C_{11} + C_{22} - \frac{C_{11}C_{22} - C_{12}^2}{C_{44}}\right)c^2s^2 - C_{12}(c^4 + s^4)}{C_{11}s^4 + C_{22}c^4 + \left(\frac{C_{11}C_{22} - C_{12}^2}{C_{44}} - 2C_{12}\right)c^2s^2}$$

where  $c = \cos \theta$  and  $s = \sin \theta$ . For the B<sub>2</sub>S monolayer, the calculated  $E(\theta)$  and  $\nu(\theta)$  are depicted in the polar diagrams in Figure 3. The diagrams show that both the Young's modulus

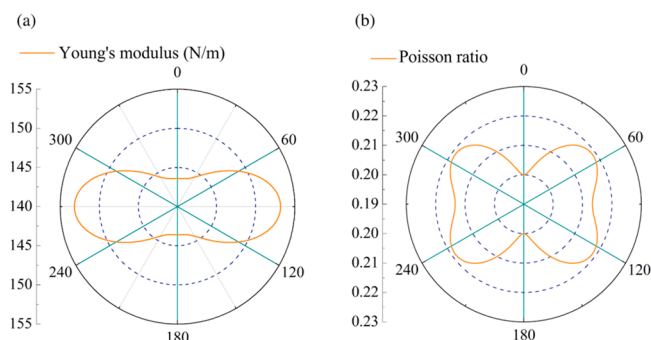


**Figure 3.** Polar diagrams for the (a) Young's modulus and (b) Poisson ratio of the B<sub>2</sub>S monolayer.

and Poisson ratio are anisotropic. The lowest Young's modulus is 143 N·m<sup>-1</sup>, which is much larger than that of silicene<sup>58</sup> (62 N·m<sup>-1</sup>) and MoS<sub>2</sub> monolayer (129 N·m<sup>-1</sup>),<sup>59</sup> confirming the strong bonding in the flat monolayered B<sub>2</sub>S sheet. This anisotropic characteristic originates from the unique arrangement of the boron and sulfur atoms in this sheet, which affects not only its mechanical properties but also its electronic properties.

After confirming the structure stability of the B<sub>2</sub>S monolayer, we calculate its electronic band structures and density of states (DOS) to explore the electronic properties. As presented in Figure 4a, the PBE results show that there are two bands crossing each other linearly at the Fermi level, indicating the existence of a zero-gap Dirac cone. To confirm the result, we

use the HSE06 functional to obtain more accurate band structures; as shown in Figure 4a, the Dirac cone still exists. We further study the effect of spin-orbit coupling (SOC) on the electronic structure of B<sub>2</sub>S. The SOC effect is so small that no observable band gap occurred because both B and S are light elements. To get insight into the formation of the zero-energy-gap state, we analyze the symmetry of the B<sub>2</sub>S monolayer. We find that the monolayer possesses space and time reversion symmetry and obeys the even-atom-number rule as most Dirac materials,<sup>60</sup> which leads to a constrained Hamiltonian and makes it possible to achieve a Dirac cone in this 2D system.

In particular, the Dirac cone has different slopes along the  $k_x$  and  $k_y$  directions, which means that the Dirac Fermions transport with different velocities in different directions.<sup>61</sup> To get a more clear observation of the anisotropic Dirac cone, we calculate the three-dimensional (3D) band structures of the B<sub>2</sub>S monolayer. The results displayed in Figure 5a,b show the presence of a distorted Dirac cone, implying direction-dependent Fermi velocities in this sheet. By a linear fitting of the band, we obtain the Fermi velocity ( $V_f = \partial E / \partial (\hbar k)$ ) of the Dirac Fermions in B<sub>2</sub>S. The Fermi velocity is  $6.7 \times 10^5$  m/s along the  $k_x$  direction and  $4.8 \times 10^5$  m/s along the  $k_y$  direction, which is comparable to that of graphene ( $8.0 \times 10^5$  m/s). Both the high and direction-dependent Fermi velocities imply the great potential for direction-dependent quantum information devices.

To explore the origin of the Dirac point, we calculate the projected density of states (PDOS) (Figure 4b), atom-decomposed (Figure 6a,b), and orbital-decomposed (Figure 6c–f) band structures of the B<sub>2</sub>S monolayer. The orbital-decomposed and atom-decomposed band structures clearly show that the bands near the Fermi level originate from the  $p_z$  orbitals. Therefore, it is possible to model the Dirac cone structure using a simple TB Hamiltonian for these  $p_z$  orbitals.

By using the WANNIER90 package, we can describe the electronic structure of B<sub>2</sub>S in terms of the maximally localized Wannier functions (MLWFs) instead of the extended Bloch functions. The tight-binding Hamiltonian for the B<sub>2</sub>S monolayer in a MLWF basis set is modeled as  $\hat{H} = \sum_i \varepsilon_i \hat{c}_i^\dagger \hat{c}_i + \sum_{i \neq j} t_{ij} \hat{c}_i^\dagger \hat{c}_j$ , where  $\varepsilon_i$  is the on-site energy,  $t_{ij}$  the hopping integral, and  $\hat{c}_i^\dagger \hat{c}_j$  the Fermion creation and annihilation operators at site  $i$ . We consider only the  $p_z$  orbitals in our TB model because the dominant contributions to the Dirac cone are from the  $p_z$  orbitals of B and S atoms, as shown in Figure 6.



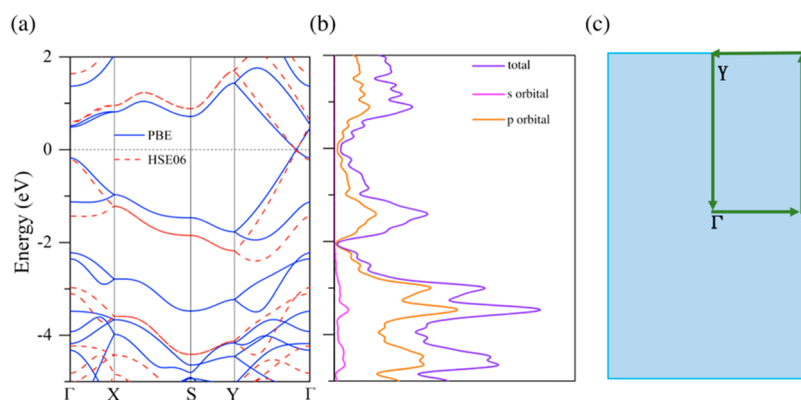


**Figure 4.** (a) Electronic band structure calculated by using the PBE (blue lines) and HSE06 (red dashed lines) functional. (b) Density of states (DOS) and projected DOS calculated at the PBE level. (c) Brillouin Zone and the high-symmetry path of the  $B_2S$  monolayer.

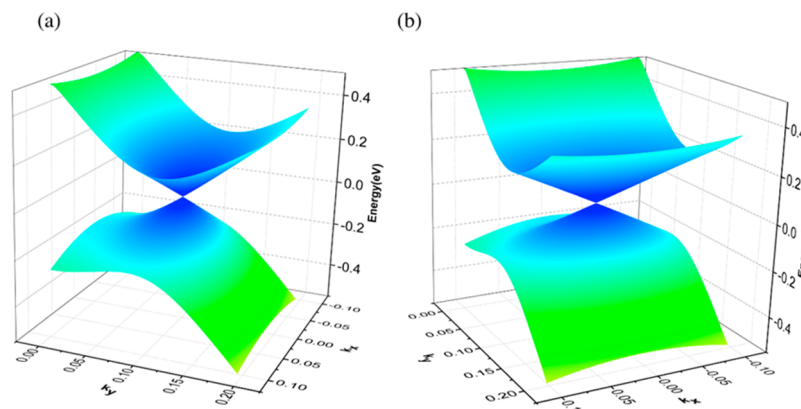


**Figure 5.** 3D electronic band structure of  $B_2S$  near the Fermi level calculated by using the PBE functional.

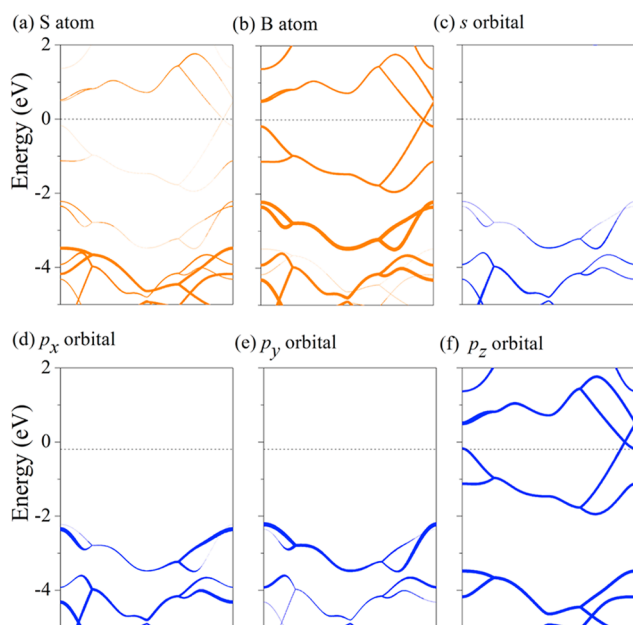


**Figure 6.** (a and b) Atom-decomposed band structures calculated by PBE functional. (c–f) Orbital-decomposed band structures calculated by PBE functional.

Including all the hoppings with hopping integral greater than  $10^{-6}$ , a relatively accurate band structure is obtained, which is in good agreement with that of the calculations at the PBE level,

as shown in Figure 7a. We then analyze the onsite-energies and hopping integrals between the different  $p_z$  orbitals obtained

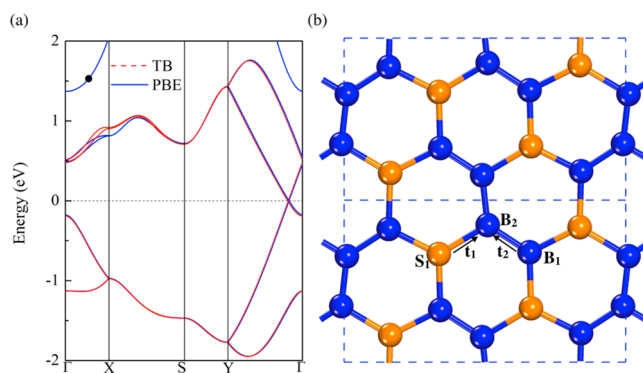


**Figure 7.** (a) Band structure calculated by using the TB model and PBE functional. (b) Hopping integral parameters of the  $B_2S$  monolayer.

using the TB model. The onsite energy is the energy of an electron sitting in a specific orbital in the presence of its neighboring atoms, whereas the hopping energies are proportional to the frequency of the electron jumping from one state to another. As shown in Figure 7b, there are two kinds of chemical environments of B atom and one chemical environment of S atom in the  $B_2S$  monolayer, denoted as  $B_1$ ,  $B_2$ , and  $S_1$ , respectively.

The onsite energy of a S atom is 6.4 eV, while that for a B atom is 5.4 eV, which means that the S atoms are more likely to attract electrons. This is also confirmed by the Bader charge analysis.<sup>62</sup> It is found that the S atom gains 1.3 electrons, while the B atom loses 0.65 electrons on average. These results are consistent with the experiential view in chemistry that sulfur has a larger electronegativity than boron. An analysis of the hopping energies obtained using our TB model reveals there are two major hopping parameters, denoted as  $t_1$  and  $t_2$  in Figure 7b. The value of  $t_2$  (1.7) is larger than that of  $t_1$  (0.8), because the  $p_z$  orbitals of  $B_2$  and  $B_1$  match each other better, resulting in greater orbital overlap between them. This analysis also uncovers the reason for the anisotropic Dirac cone, which is due to the different electron-transfer abilities between these neighboring atoms that breaks the particle–hole symmetry in the  $B_2S$  monolayer, resulting in an anisotropic Dirac cone.<sup>63</sup>

In summary, by using the PSO-based global structure search method and first-principles calculations with a tight binding model, we have identified a novel  $B_2S$  monolayer, which is stable dynamically, thermally, and mechanically. The geometry of the  $B_2S$  monolayer is very intriguing because B has one electron less than C, the graphene geometry is unstable for a pure B sheet, which can be stabilized by S leading to a honeycomb structure similar to that of graphene, silicene, germanene, and stanene. However, the  $B_2S$  monolayer is electronically different from these honeycomb sheets, showing an anisotropic Dirac cone along the high-symmetry path with anisotropic Fermi velocities in the same order of magnitude compared with that of graphene, thus exhibiting great potential for  $B_2S$  to be applied in direction-dependent electronic devices with high speed and low dissipation. We hope this study stimulates experimental efforts to synthesize the predicted new honeycomb monolayer to enrich the anisotropic Dirac cone materials.

## AUTHOR INFORMATION

### Corresponding Author

\*E-mail: qianwang2@pku.edu.cn.

### ORCID

Yu Zhao: 0000-0001-9958-5421

Cunzhi Zhang: 0000-0002-4562-535X

Qian Wang: 0000-0002-9766-4617

### Notes

The authors declare no competing financial interest.

## ACKNOWLEDGMENTS

This work is partially supported by grants from the National Key Research and Development Program of China (2016YFE0127300, 2017YFA0205003), the National Natural Science Foundation of China (NSFC-51471004, NSFC-21773004), and the National Training Program of Innovation for Undergraduates of China and is supported by the High Performance Computing Platform of Peking University, China.

## REFERENCES

- (1) Geim, A. K.; Novoselov, K. S. The Rise of Graphene. *Nat. Mater.* **2007**, *6*, 183.
- (2) Bolotin, K. I.; Sikes, K. J.; Jiang, Z.; Klima, M.; Fudenberg, G.; Hone, J.; Kim, P.; Stormer, H. L. Ultrahigh Electron Mobility in Suspended Graphene. *Solid State Commun.* **2008**, *146*, 351–355.
- (3) Jose, D.; Datta, A. Understanding of the Buckling Distortions in Silicene. *J. Phys. Chem. C* **2012**, *116*, 24639–24648.
- (4) Cahangirov, S.; Topsakal, M.; Aktürk, E.; Şahin, H.; Ciraci, S. Two- and One-Dimensional Honeycomb Structures of Silicon and Germanium. *Phys. Rev. Lett.* **2010**, *102*, 236804.
- (5) Chen, J.; Xi, J.; Wang, D.; Shuai, Z. Carrier Mobility in Graphyne Should Be Even Larger Than That in Graphene: A Theoretical Prediction. *J. Phys. Chem. Lett.* **2013**, *4*, 1443.
- (6) Zhao, M.; Dong, W.; Wang, A. Two-Dimensional Carbon Topological Insulators Superior to Graphene. *Sci. Rep.* **2013**, *3*, 3532.
- (7) Xu, L. C.; Wang, R. Z.; Miao, M. S.; Wei, X. L.; Chen, Y. P.; Yan, H.; Lau, W. M.; Liu, L. M.; Ma, Y. M. Two Dimensional Dirac Carbon Allotropes from Graphene. *Nanoscale* **2014**, *6*, 1113–1118.
- (8) Wang, Z.; Zhou, X. F.; Zhang, X.; Zhu, Q.; Dong, H.; Zhao, M.; Oganov, A. R. Phagraphene: A Low-Energy Graphene Allotrope Composed of 5–6–7 Carbon Rings with Distorted Dirac Cones. *Nano Lett.* **2015**, *15*, 6182–6186.
- (9) Zhou, X. F.; et al. Semimetallic Two-Dimensional Boron Allotrope with Massless Dirac Fermions. *Phys. Rev. Lett.* **2014**, *112*, 0855502.
- (10) Zhang, H.; Xie, Y.; Zhang, Z.; Zhong, C.; Li, Y.; Chen, Z.; Chen, Y. Dirac Nodal Lines and Tilted Semi-Dirac Cones Coexisting in a Striped Boron Sheet. *J. Phys. Chem. Lett.* **2017**, *8*, 1707.
- (11) Qin, X.; Wu, Y.; Liu, Y.; Chi, B.; Li, X.; Wang, Y.; Zhao, X. Origins of Dirac Cone Formation in Ab 3 and a 3 B (a, B = C, Si, and Ge) Binary Monolayers. *Sci. Rep.* **2017**, *7*, 10546.
- (12) Pu, C.; Zhou, D.; Li, Y.; Liu, H.; Chen, Z.; Wang, Y.; Ma, Y. Two-Dimensional  $C_4N$  Global Minima: Unique Structural Topologies and Nanoelectronic Properties. *J. Phys. Chem. C* **2017**, *121*, 2669.
- (13) Wang, B.; Yuan, S.; Li, Y.; Shi, L.; Wang, J. A New Dirac Cone Material: A Graphene-Like  $Be_3C_2$  Monolayer. *Nanoscale* **2017**, *9*, 5577–5582.
- (14) Feng, B.; Zhang, J.; Zhong, Q.; Li, W.; Li, S.; Li, H.; Cheng, P.; Meng, S.; Chen, L.; Wu, K. Experimental Realization of Two-Dimensional Boron Sheets. *Nat. Chem.* **2016**, *8*, 563.
- (15) Feng, B.; Zhang, J.; Liu, R.-Y.; Iimori, T.; Lian, C.; Li, H.; Chen, L.; Wu, K.; Meng, S.; Komori, F.; et al. Direct Evidence of Metallic Bands in a Monolayer Boron Sheet. *Phys. Rev. B: Condens. Matter Phys.* **2016**, *94*, 041408.
- (16) Cheng, T.; Lang, H.; Li, Z.; Liu, Z.; Liu, Z. Anisotropic Carrier Mobility in Two-Dimensional Materials with Tilted Dirac Cones: Theory and Application. *Phys. Chem. Chem. Phys.* **2017**, *19*, 23942–23950.
- (17) Feng, B.; Zhang, J.; Ito, S.; Arita, M.; Cheng, C.; Chen, L.; Wu, K.; Komori, F.; Sugino, O.; Miyamoto, K. Discovery of 2d Anisotropic Dirac Cones. *Adv. Mater.* **2018**, *30*, 1704025.
- (18) Zhang, H.; Li, Y.; Hou, J.; Du, A.; Chen, Z. Dirac State in the  $FeB_2$  Monolayer with Graphene-Like Boron Sheet. *Nano Lett.* **2016**, *16*, 6124–6129.
- (19) Zhang, L. Z.; Wang, Z. F.; Du, S. X.; Gao, H. J.; Liu, F. Prediction of a Dirac State in Monolayer  $TiB_2$ . *Phys. Rev. B: Condens. Matter Phys.* **2014**, *90*, 161402.
- (20) Alexandrova, A. N.; Zhai, H. J.; Wang, L. S.; Boldyrev, A. I. Molecular Wheel  $B-8(2-)$  as a New Inorganic Ligand. Photoelectron Spectroscopy and Ab Initio Characterization of  $LiB_8$ . *Inorg. Chem.* **2004**, *43*, 3552–3554.
- (21) Alexandrova, A. N.; Boldyrev, A. I.; Zhai, H. J.; Wang, L. S. Photoelectron Spectroscopy and Ab Initio Study of the Doubly Antiaromatic  $B-6(2-)$  Dianion in the  $LiB_6$  Cluster. *J. Chem. Phys.* **2005**, *122*, 054313.
- (22) An, W.; Bulusu, S.; Gao, Y.; Zeng, X. C. Relative Stability of Planar Versus Double-Ring Tubular Isomers of Neutral and Anionic Boron Cluster  $B-20$  and  $B-20(-)$ . *J. Chem. Phys.* **2006**, *124*, 154310.
- (23) Sergeeva, A. P.; Zubarev, D. Y.; Zhai, H.-J.; Boldyrev, A. I.; Wang, L.-S. Photoelectron Spectroscopic and Theoretical Study of  $B-16(-)$  and  $B-16(2-)$ : An All-Boron Naphthalene. *J. Am. Chem. Soc.* **2008**, *130*, 7244.
- (24) Huang, W.; Sergeeva, A. P.; Zhai, H.-J.; Averkiev, B. B.; Wang, L.-S.; Boldyrev, A. I. A Concentric Planar Doubly Pi-Aromatic  $B-19(-)$  Cluster. *Nat. Chem.* **2010**, *2*, 202–206.

- (25) Sergeeva, A. P.; Averkiev, B. B.; Zhai, H.-J.; Boldyrev, A. I.; Wang, L.-S. All-Boron Analogues of Aromatic Hydrocarbons: B-17(–) and B-18(–). *J. Chem. Phys.* **2011**, *134*, 224304.
- (26) Sergeeva, A. P.; Piazza, Z. A.; Romanescu, C.; Li, W.-L.; Boldyrev, A. I.; Wang, L.-S. B-22(–) and B-23(–): All-Boron Analogues of Anthracene and Phenanthrene. *J. Am. Chem. Soc.* **2012**, *134*, 18065–18073.
- (27) Piazza, Z. A.; Li, W.-L.; Romanescu, C.; Sergeeva, A. P.; Wang, L.-S.; Boldyrev, A. I. A Photoelectron Spectroscopy and Ab Initio Study of B21(–): Negatively Charged Boron Clusters Continue to Be Planar at 21. *J. Chem. Phys.* **2012**, *136*, 104310.
- (28) Popov, I. A.; Piazza, Z. A.; Li, W.-L.; Wang, L.-S.; Boldyrev, A. I. A Combined Photoelectron Spectroscopy and Ab Initio Study of the Quasi-Planar B24(–) Cluster. *J. Chem. Phys.* **2013**, *139*, 144307–144307.
- (29) Morgan, R. S.; Tatsch, C. E.; Gushard, R. H.; Mcadon, J. M.; Warne, P. K. Chains of Alternating Sulfur and  $\Pi$ -Bonded Atoms in Eight Small Proteins. *Int. J. Pept. Protein Res.* **1978**, *11*, 209–217.
- (30) Byskov, L. S.; Hammer, B.; Nørskov, J. K.; Clausen, B. S.; Topsøe, H. Sulfur Bonding in MoS<sub>2</sub> and Co-MoS Structures. *Catal. Lett.* **1997**, *47*, 177–182.
- (31) Murray, J. S.; Lane, P.; Clark, T.; Politzer, P.  $\Sigma$ -Hole Bonding: Molecules Containing Group VI Atoms. *J. Mol. Model.* **2007**, *13*, 1033–1038.
- (32) Zhang, C.; Sun, Q. A Honeycomb Ben<sub>2</sub> Sheet with a Desirable Direct Band Gap and High Carrier Mobility. *J. Phys. Chem. Lett.* **2016**, *7*, 2664–2670.
- (33) Tarruell, L.; Greif, D.; Uehlinger, T.; Jotzu, G.; Esslinger, T. Creating, Moving and Merging Dirac Points with a Fermi Gas in a Tunable Honeycomb Lattice. *Nature* **2012**, *483*, 302.
- (34) Malko, D.; Neiss, C.; Vines, F.; Gorling, A. Competition for Graphene: Graphynes with Direction-Dependent Dirac Cones. *Phys. Rev. Lett.* **2012**, *108*, 086804.
- (35) Trescher, M.; Sbierski, B.; Brouwer, P. W.; Bergholtz, E. J. Quantum Transport in Dirac Materials: Signatures of Tilted and Anisotropic Dirac and Weyl Cones. *Phys. Rev. B: Condens. Matter Mater. Phys.* **2015**, *91*, 115135.
- (36) Goerbig, M.; Fuchs, J.-N.; Montambaux, G.; Piéchon, F. Tilted Anisotropic Dirac Cones in Quinoid-Type Graphene and A–(Bedt-Tft) 2 I 3. *Phys. Rev. B: Condens. Matter Mater. Phys.* **2008**, *78*, 045415.
- (37) Wang, Y.; Lv, J.; Li, Z.; Ma, Y. Calypso: A Method for Crystal Structure Prediction. *Comput. Phys. Commun.* **2012**, *183*, 2063–2070.
- (38) Zhu, L.; Liu, H.; Pickard, C. J.; Zou, G.; Ma, Y. Reactions of Xenon with Iron and Nickel Are Predicted in the Earth's Inner Core. *Nat. Chem.* **2014**, *6*, 644.
- (39) Lu, S.; Wang, Y.; Liu, H.; Miao, M.-s.; Ma, Y. Self-Assembled Ultrathin Nanotubes on Diamond (100). *Nat. Commun.* **2014**, *5*, 3666.
- (40) Miao, M.-s. Caesium in High Oxidation States and as a P-Block Element. *Nat. Chem.* **2013**, *5*, 846.
- (41) Li, Q.; Zhou, D.; Zheng, W.; Ma, Y.; Chen, C. Global Structural Optimization of Tungsten Borides. *Phys. Rev. Lett.* **2013**, *110*, 136403.
- (42) Lu, C.; Miao, M.; Ma, Y. Structural Evolution of Carbon Dioxide under High Pressure. *J. Am. Chem. Soc.* **2013**, *135*, 14167–14171.
- (43) Kresse, G.; Furthmüller, J. Efficient Iterative Schemes for Ab Initio Total-Energy Calculations Using a Plane-Wave Basis Set. *Phys. Rev. B: Condens. Matter Mater. Phys.* **1996**, *54*, 11169.
- (44) Blöchl, P. E. Projector Augmented-Wave Method. *Phys. Rev. B: Condens. Matter Mater. Phys.* **1994**, *50*, 17953.
- (45) Pack, J. D.; Monkhorst, H. J. "Special points for Brillouin-zone integrations"—a reply. *Phys. Rev. B* **1977**, *16*, 1748–1749.
- (46) Perdew, J. P.; Burke, K.; Ernzerhof, M. Errata: Generalized Gradient Approximation Made Simple. *Phys. Rev. Lett.* **1996**, *77*, 3865.
- (47) Perdew, J. P.; Burke, K.; Ernzerhof, M. Generalized Gradient Approximation Made Simple. *Phys. Rev. Lett.* **1996**, *77*, 3865.
- (48) Heyd, J.; Scuseria, G. E.; Ernzerhof, M. Hybrid Functionals Based on a Screened Coulomb Potential. *J. Chem. Phys.* **2003**, *118*, 8207–8215.
- (49) Paier, J.; Marsman, M.; Hummer, K.; Kresse, G.; Gerber, I. C.; Ángyán, J. G. Erratum: "Screened Hybrid Density Functionals Applied to Solids" [J. Chem. Phys. **124**, 154709 (2006)]. *J. Chem. Phys.* **2006**, *124*, 154709.
- (50) Togo, A.; Tanaka, I. First Principles Phonon Calculations in Materials Science. *Scr. Mater.* **2015**, *108*, 1–5.
- (51) Mostofi, A. A.; Yates, J. R.; Lee, Y. S.; Souza, I.; Vanderbilt, D.; Marzari, N. Wannier90: A Tool for Obtaining Maximally-Localised Wannier Functions. *Comput. Phys. Commun.* **2008**, *178*, 685–699.
- (52) Giannozzi, P.; Baroni, S.; Bonini, N.; Calandra, M.; Car, R.; Cavazzoni, C.; Ceresoli, D.; Chiarotti, G. L.; Cococcioni, M.; Dabo, I.; et al. Quantum Espresso: A Modular and Open-Source Software Project for Quantum Simulations of Materials. *J. Phys.: Condens. Matter* **2009**, *21*, 395502.
- (53) Blöchl, P. E. Projector Augmented-Wave Method. *Phys. Rev. B: Condens. Matter Mater. Phys.* **1994**, *50*, 17953.
- (54) Jain, A.; Ong, S. P.; Hautier, G.; Chen, W.; Richards, W. D.; Dacek, S.; Cholia, S.; Gunter, D.; Skinner, D.; Ceder, G.; et al. Commentary: The Materials Project: A Materials Genome Approach to Accelerating Materials Innovation. *APL Mater.* **2013**, *1*, 011002.
- (55) Nosé, S. A. Unified Formulation of the Constant Temperature Molecular Dynamics Methods. *J. Chem. Phys.* **1984**, *81*, 511–519.
- (56) Mouhat, F.; Coudert, F.-X. Necessary and Sufficient Elastic Stability Conditions in Various Crystal Systems. *Phys. Rev. B: Condens. Matter Mater. Phys.* **2014**, *90*, 224104.
- (57) Cadelano, E.; Palla, P. L.; Giordano, S.; Colombo, L. Elastic Properties of Hydrogenated Graphene. *Phys. Rev. B: Condens. Matter Mater. Phys.* **2010**, *82*, 235414.
- (58) Ding, Y.; Wang, Y. Density Functional Theory Study of the Silicene-Like Six and Xsi<sub>3</sub> (X = B, C, N, Al, P) Honeycomb Lattices: The Various Buckled Structures and Versatile Electronic Properties. *J. Phys. Chem. C* **2013**, *117*, 18266–18278.
- (59) Cooper, R. C.; Lee, C.; Marianetti, C. A.; Wei, X.; Hone, J.; Kysar, J. W. Nonlinear Elastic Behavior of Two-Dimensional Molybdenum Disulfide. *Phys. Rev. B: Condens. Matter Mater. Phys.* **2013**, *87*, 035423.
- (60) Wang, J.; Deng, S.; Liu, Z.; Liu, Z. The Rare Two-Dimensional Materials with Dirac Cones. *Natl. Sci. Rev.* **2015**, *2*, 22–39.
- (61) Zhou, X. F.; Wang, H. T. Low-Dimensional Boron: Searching for Dirac Materials. *Advances in Physics: X* **2016**, *1*, 412.
- (62) Tang, W.; Sanville, E.; Henkelman, G. A Grid-Based Bader Analysis Algorithm without Lattice Bias. *J. Phys.: Condens. Matter* **2009**, *21*, 084204.
- (63) Lu, H.-Y.; Cuamba, A. S.; Lin, S.-Y.; Hao, L.; Wang, R.; Li, H.; Zhao, Y.; Ting, C. Tilted Anisotropic Dirac Cones in Partially Hydrogenated Graphene. *Phys. Rev. B: Condens. Matter Mater. Phys.* **2016**, *94*, 195423.